Theoretical comparison of three X-ray phase-contrast imaging techniques: propagation-based imaging, analyzer-based imaging and grating interferometry

P.C. Diemoz,[1,2,*] A. Bravin,[2] and P. Coan[1,3]

[1] *Faculty of Physics, Ludwig-Maximilians-University München, 85748 Garching, Germany*
[2] *European Synchrotron Radiation Facility, 38043 Grenoble, France*
[3] *Faculty of Medicine, Ludwig-Maximilians-University München, 81377 Munich, Germany*
*p.diemoz@ucl.ac.uk

Abstract: Various X-ray phase-contrast imaging techniques have been developed and applied over the last twenty years in different domains, such as material sciences, biology and medicine. However, no comprehensive inter-comparison exists in the literature. We present here a theoretical study that compares three among the most used techniques: propagation-based imaging (PBI), analyzer-based imaging (ABI) and grating interferometry (GI). These techniques are evaluated in terms of signal-to-noise ratio, figure of merit and spatial resolution. Both area and edge signals are considered. Dependences upon the object properties (absorption, phase shift) and the experimental acquisition parameters (energy, system point-spread function etc.) are derived and discussed. The results obtained from this analysis can be used as the reference for determining the most suitable technique for a given application.

OCIS codes: (110.7440) X-ray imaging; (110.2990) Image formation theory; (100.2960) Image analysis; (110.4980) Partial coherence in imaging.

References and links

1. M. Born and E. Wolf, *Principles of Optics: Electromagnetic Theory of Propagation, Interference and Diffraction of Light* (Cambridge University Press, Cambridge, 1999).
2. U. Bonse and M. Hart, "An X-ray interferometer," Appl. Phys. Lett. **6**(8), 155–156 (1965).
3. A. Momose, T. Takeda, Y. Itai, and K. Hirano, "Phase-contrast X-ray computed tomography for observing biological soft tissues," Nat. Med. **2**(4), 473–475 (1996).
4. A. Snigirev, I. Snigireva, V. Kohn, S. Kuznetsov, and I. Schelokov, "On the possibility of x-ray phase contrast microimaging by coherent high-energy synchrotron radiation," Rev. Sci. Instrum. **66**(12), 5486–5492 (1995).
5. S. W. Wilkins, T. E. Gureyev, D. Gao, A. Pogany, and A. W. Stevenson, "Phase-contrast imaging using polychromatic hard X-rays," Nature **384**(6607), 335–338 (1996).
6. E. Förster, K. Goetz, and P. Zaumseil, "Double crystal diffractometry for the characterization of targets for laser fusion experiments," Krist. Tech. **15**(8), 937–945 (1980).
7. D. Chapman, W. Thomlinson, R. E. Johnston, D. Washburn, E. Pisano, N. Gmur, Z. Zhong, R. Menk, F. Arfelli, and D. Sayers, "Diffraction enhanced x-ray imaging," Phys. Med. Biol. **42**(11), 2015–2025 (1997).
8. A. Bravin, "Exploiting the X-ray refraction contrast with an analyser: the state of the art," J. Phys. D Appl. Phys. **36**(10A), A24–A29 (2003).
9. C. David, B. Nöhammer, H. Solak, and E. Ziegler, "Differential X-ray phase contrast imaging using a shearing interferometer," Appl. Phys. Lett. **81**(17), 3287–3289 (2002).
10. T. Weitkamp, A. Diaz, C. David, F. Pfeiffer, M. Stampanoni, P. Cloetens, and E. Ziegler, "X-ray phase imaging with a grating interferometer," Opt. Express **13**(16), 6296–6304 (2005).
11. F. Pfeiffer, T. Weitkamp, O. Bunk, and C. David, "Phase retrieval and differential phase-contrast imaging with low-brilliance X-ray sources," Nat. Phys. **2**(4), 258–261 (2006).
12. A. Olivo, K. Ignatyev, P. R. T. Munro, and R. D. Speller, "Noninterferometric phase-contrast images obtained with incoherent x-ray sources," Appl. Opt. **50**(12), 1765–1769 (2011).
13. E. Castelli, M. Tonutti, F. Arfelli, R. Longo, E. Quaia, L. Rigon, D. Sanabor, F. Zanconati, D. Dreossi, A. Abrami, E. Quai, P. Bregant, K. Casarin, V. Chenda, R. H. Menk, T. Rokvic, A. Vascotto, G. Tromba, and M. A.

Cova, "Mammography with synchrotron radiation: first clinical experience with phase-detection technique," Radiology **259**(3), 684–694 (2011).

14. P. Coan, F. Bamberg, P. C. Diemoz, A. Bravin, K. Timpert, E. Mützel, J. G. Raya, S. Adam-Neumair, M. F. Reiser, and C. Glaser, "Characterization of osteoarthritic and normal human patella cartilage by computed tomography X-ray phase-contrast imaging: a feasibility study," Invest. Radiol. **45**(7), 437–444 (2010).

15. G. Schulz, T. Weitkamp, I. Zanette, F. Pfeiffer, F. Beckmann, C. David, S. Rutishauser, E. Reznikova, and B. Mueller, "High-resolution tomographic imaging of a human cerebellum: comparison of absorption and grating-based phase contrast," J. R. Soc. Interface **7**(53), 1665–1676 (2010).

16. E. Pagot, S. Fiedler, P. Cloetens, A. Bravin, P. Coan, K. Fezzaa, J. Baruchel, J. Härtwig, K. von Smitten, M. Leidenius, M. L. Karjalainen-Lindsberg, and J. Keyriläinen, "Quantitative comparison between two phase contrast techniques: diffraction enhanced imaging and phase propagation imaging," Phys. Med. Biol. **50**(4), 709–724 (2005).

17. M. R. Teague, "Irradiance moments - their propagation and use for unique retrieval of phase," J. Opt. Soc. Am. **72**(9), 1199–1209 (1982).

18. T. E. Gureyev, Y. I. Nesterets, A. W. Stevenson, P. R. Miller, A. Pogany, and S. W. Wilkins, "Some simple rules for contrast, signal-to-noise and resolution in in-line x-ray phase-contrast imaging," Opt. Express **16**(5), 3223–3241 (2008).

19. P. Coan, E. Pagot, S. Fiedler, P. Cloetens, J. Baruchel, and A. Bravin, "Phase-contrast X-ray imaging combining free space propagation and Bragg diffraction," J. Synchrotron Radiat. **12**(2), 241–245 (2005).

20. Y. I. Nesterets, P. Coan, T. E. Gureyev, A. Bravin, P. Cloetens, and S. W. Wilkins, "On qualitative and quantitative analysis in analyser-based imaging," Acta Crystallogr. A **62**(4), 296–308 (2006).

21. T. E. Gureyev and S. W. Wilkins, "Regimes of X-ray phase-contrast imaging with perfect crystals," Nuovo Cimento D **19**(2-4), 545–552 (1997).

22. K. M. Pavlov, T. E. Gureyev, D. Paganin, Y. I. Nesterets, M. J. Morgan, and R. A. Lewis, "Linear systems with slowly varying transfer functions and their application to x-ray phase-contrast imaging," J. Phys. D Appl. Phys. **37**(19), 2746–2750 (2004).

23. R. Tanuma and M. Ohsawa, "Submicron-resolved X-ray topography using asymmetric-reflection magnifiers," Spectrochim. Acta, Part B **59**(10-11), 1549–1555 (2004).

24. P. C. Diemoz, P. Coan, I. Zanette, A. Bravin, S. Lang, C. Glaser, and T. Weitkamp, "A simplified approach for computed tomography with an X-ray grating interferometer," Opt. Express **19**(3), 1691–1698 (2011).

25. A. L. Evans, *The Evaluation of Medical Images* (Adam Hilger Ltd, Bristol, 1981).

26. F. Arfelli, V. Bonvicini, A. Bravin, G. Cantatore, E. Castelli, L. Dalla Palma, M. Di Michiel, R. Longo, A. Olivo, S. Pani, D. Pontoni, P. Poropat, M. Prest, A. Rashevsky, G. Tromba, and A. Vacchi, "Mammography of a phantom and breast tissue with synchrotron radiation and a linear-array silicon detector," Radiology **208**(3), 709–715 (1998).

27. S. Webb, *The Physics of Medical Imaging* (Institute of Physics Publishing, Bristol, 1988).

28. J. M. Boone, K. K. Lindfors, V. N. Cooper 3rd, and J. A. Seibert, "Scatter/primary in mammography: comprehensive results," Med. Phys. **27**(10), 2408–2416 (2000).

29. J. Persliden and G. A. Carlsson, "Scatter rejection by air gaps in diagnostic radiology. Calculations using a Monte Carlo collision density method and consideration of molecular interference in coherent scattering," Phys. Med. Biol. **42**(1), 155–175 (1997).

30. M. Sanchez del Rio, C. Ferrero, and V. Mocella, "Computer simulations of bent perfect crystal diffraction profiles," Proc. SPIE **3152**, 312–323 (1997), http://www.esrf.eu/UsersAndScience/Experiments/TBS/SciSoft/xop2.3.

31. T. Matsushita and H. Hashizume, "X-Ray monochromators," in *Handbook on Synchrotron Radiation*, E. Koch, ed. (North Holland Publishing Company, New York, 1983), pp. 261–314.

1. Introduction

In conventional X-ray imaging, the contrast is generated by variations of the X-ray attenuation that arise from differences in the thickness, composition and density of the imaged object. These variations, however, can be very tiny when imaging samples composed by low Z elements like soft biological tissues. Moreover, in the case of clinical or in-vivo imaging, the radiation dose (and therefore the photon fluence) has to be kept as low as possible. As a result, the obtained image contrast may be not sufficient for the complete discrimination and characterization of the healthy and diseased tissues in a given sample/patient.

With the aim of overcoming the intrinsic limitations of attenuation-based X-ray imaging, a number of phase-contrast techniques have been developed and applied over the last twenty years. Unlike conventional X-ray methods, these techniques are not only sensitive to the attenuation, but also to the phase shift that X-rays, as all electromagnetic waves, experience when passing through the matter. The propagation of X-rays in matter can be mathematically described in terms of the complex index of refraction $n = 1 - \delta + i\beta$, whose real part δ and

imaginary part β are related to the phase shift and to the X-ray attenuation in the object, respectively [1]. Since δ is orders of magnitude higher than β in the hard X-rays range, the phase shift can be significant even for small details characterized by a weak amplitude modulation (i.e. attenuation). Therefore, the achievable contrast for soft biological tissues can be greatly increased.

Various techniques have been developed to exploit the phase contrast in the X-ray regime. They can be classified into five main categories: the interferometric methods based on the use of crystals [2, 3], the propagation-based imaging (PBI) methods [4, 5], the analyzer-based imaging (ABI) methods [6–8], the grating interferometric (GI) [9–11] and the grating non-interferometric methods [12].

In this article, we will focus on PBI, ABI and GI, the most largely presented techniques in the literature in the past years. These methods differ not only for their experimental setup and requirements in terms of the X-ray beam spatial and temporal coherence, but also for the nature and amplitude of the provided image signal, and for the amount of radiation dose that is delivered to the sample. These phase-contrast modalities (in particular PBI and ABI) have been extensively investigated in preclinical and clinical trials to access their potential for biomedical imaging, in subjects as diverse as mammography [13], cartilage imaging [14] and brain imaging [15]. Despite the large number of publications in the field of phase contrast, very few attempts have been made to compare these different methods [16], and a complete qualitative and quantitative comparison is still missing in the literature.

We here present a theoretical comparison of PBI, ABI and GI by examining key parameters as the spatial resolution, the signal-to-noise ratio, the delivered radiation dose and the figure-of-merit. The advantages and drawbacks of each method and the consequences in biomedical applications will be also discussed.

In the next section, the main features, formulas and experimental requirements of the PBI, ABI and GI techniques are briefly reviewed. In section 2.1 the various contributions to spatial resolution are summarized. In section 3, the notions of signal-to-noise ratio (SNR) and figure-of-merit (FoM) for area and edge signals are introduced, and general expressions for these quantities derived. Simple expressions that relate the FoM with the acquisition parameters for each of the considered techniques are finally obtained and compared in section 4.

2. Brief description of PBI, ABI and GI techniques

In order to simplify the description, we will consider only the case of monochromatic radiation, characterized by a definite wavelength λ, and the typical 1-dimensional (1-D) implementation of ABI and GI; extension of the formalism to the 2-D case is straightforward.

1. *Propagation-based imaging (PBI)* is the method with the simplest experimental setup. It requires that the sample is irradiated with highly spatially coherent radiation and that the detector is positioned at a sufficient distance r from the sample; no optical elements are needed between the sample and the detector. Thanks to Fresnel diffraction, the differences in phase shift introduced by the object onto the beam lead to a measurable intensity modulation onto the detector [1]. This intensity can be expressed, in the near-field diffraction regime, by the transport of intensity equation (TIE) [17]. The near-field regime approximation is valid for sufficiently small propagation distances and for objects introducing a slowly varying phase shift in the plane (x,y) transversal to the optical axis z [18]. In the case of additional slowly varying object absorption, the TIE can be written as (for sake of simplicity the spatial variables are omitted):

$$I_{PBI} = M^{-2}I_0 T\left(1 - \frac{\lambda d}{2\pi}\nabla_\perp^2 \phi\right) \qquad (1)$$

where $M = (r+l)/l$, with l being the source-to-sample distance, is the magnification factor, which takes into account the beam divergence; I_0 indicates the intensity incident onto the object; $T = \exp\left(-\int dz\, \mu_{obj}\right)$ is the object transmission and μ is the linear attenuation coefficient; $d = r/M$ is the so-called defocusing distance and ϕ is the phase shift introduced by the object. Under these approximations, the intensity modulation is thus proportional to the Laplacian of the phase shift. As an example, a typical PBI intensity profile corresponding to a pure phase object (Fig. 1(a)) is plotted in Fig. 1(b).

As shown by Wilkins and associates [5], PBI is relatively insensitive to broad beam polychromaticity. However, a high degree of spatial coherence is required, otherwise the interference fringes are rapidly smeared out.
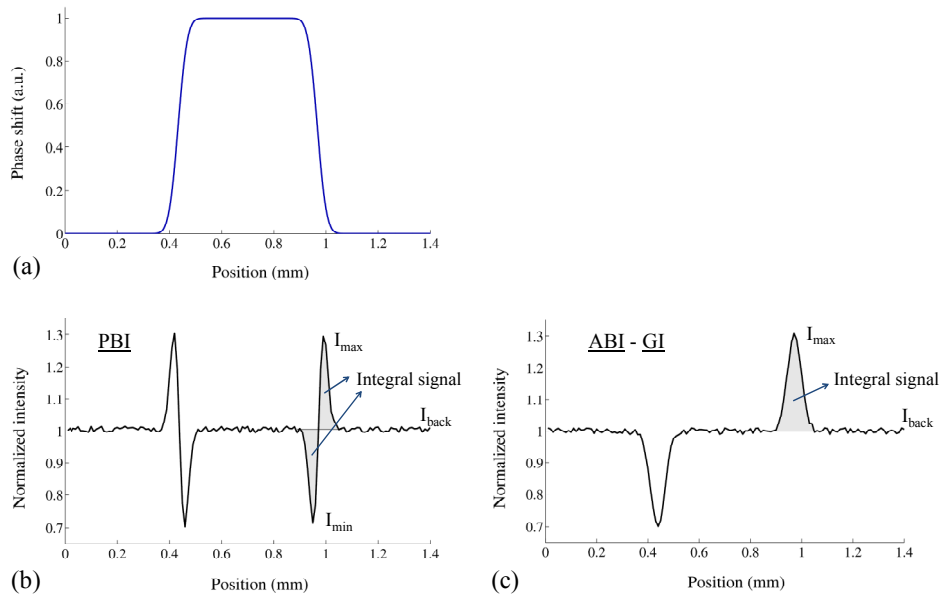

Fig. 1. (a) Profile of a pure phase object. (b) Typical corresponding PBI signal that can be calculated from Eq. (1). (c) Typical ABI / GI signal that can be calculated from Eqs. (4 and 6). Values have been normalized by the average background intensity I_{back}. Poissonian noise has been added to the theoretical profiles. Maximum (I_{max}) and minimum (I_{min}) values for the intensity at the edge, as well as the integral of the edge signal, are also drawn in the figure.

2. *Analyzer-based imaging (ABI)* makes use of a quasi-monochromatic and quasi-parallel beam (typically produced by diffraction from a perfect crystal, called the monochromator) irradiating the sample and of a perfect "analyzer" crystal placed between the sample and the detector. The analyzer acts as an angular filter of the radiation refracted and scattered by the sample. In a typical ABI setup the sample-to-detector distance is small, so that the propagation phase contrast can be neglected [19]. The general expression for the intensity recorded on the detector [20] can be greatly simplified under the geometrical optics approximation [21], which is valid if the phase of the wave incident onto the crystal is a slowly varying function over the length scales on the order of the crystal extinction length [22]. In this case the intensity for each detector pixel can then be expressed, if the crystal diffraction plane is assumed to be parallel to the (*y,z*) plane, as:

$$I_{ABI} = M^{-2} M_{asym} I_0 T\, R\left(\theta_{an} + \Delta\theta_y\right) \qquad (2)$$

where M accounts for the image magnification due to beam divergence and M_{asym} for that arising in the case of an asymmetrically-cut analyzer crystal [23], which affects only the direction y parallel to the diffraction plane. θ_{an} is the angular deviation of the crystal from the Bragg angle and $\Delta\theta_y = -\lambda/2\pi\, \partial\phi/\partial y$ is the component of the refraction angle that is parallel to the diffraction plane. R is the so-called rocking curve (RC), defined as the ratio between the intensity diffracted by the analyzer crystal and the intensity incident on it, and whose expression is given by:

$$R(\theta) = \frac{\int_\theta d\theta' f(\theta') R_M(\theta') R_{AN}(\theta - \theta')}{\int_\theta d\theta' R_M(\theta')} \qquad (3)$$

where R_M and R_{AN} are the reflectivity curves of the monochromator (M) and analyzer (AN) crystals respectively, and $f(\theta')$ is the angular distribution of photons incident onto the monochromator. If the object refraction angles are small compared to the full-width at half maximum (FWHM) of the RC, Eq. (2) can be rewritten by using a first-order Taylor approximation of the RC [7]:

$$I_{ABI} \simeq M^{-2} M_{asym} I_0 T \left[R(\theta_{an}) + R'(\theta_{an}) \Delta\theta_y \right] \qquad (4)$$

where $R'(\theta_{an})$ denotes the first derivative of the RC. In case of small refraction angles, therefore, the intensity modulation in ABI is proportional to the refraction angle itself. As an example, a typical ABI signal for a pure phase object is plotted in Fig. 1(c).

In ABI, X-rays incident on the sample must be almost parallel and monochromatic with a typical energy bandwidth, $\Delta E/E$, of a perfect crystal (10^{-4}). Due to the unavoidable loss of photons occurring in the monochromatization/collimation process in the first crystal, sources providing highly collimated and intense X-rays, like synchrotron radiation facilities, are particularly advantageous for ABI.

3. *The grating interferometry (GI)* technique consists in illuminating the imaged object with highly spatially coherent X-rays, and in analyzing the radiation transmitted through the object by using a pair of gratings [10]. The first is generally a phase grating, of period p_1, which introduces a periodic phase shift onto the beam but negligible absorption. A second absorption grating of period p_2 is then placed downstream at one of the so-called fractional Talbot distances d_{Talbot}, where the interference fringes created by the first grating give rise to the so-called self-imaging effect.

Let us assume the grating lines to be perpendicular to the axis y, and let us denote with y_G the relative position of the two gratings in this direction. The intensity incident on each detector pixel can in general be approximated by [24]:

$$I_{GI} = M^{-2} I_0 T_{GR} T \left[1 + V \sin\left(\psi + \frac{2\pi}{p_2} y_G + \frac{2\pi}{S} \Delta\theta_y \right) \right] = M^{-2} I_0 T_{GR} T\, G\left(y_G ; \Delta\theta_y \right) \quad (5)$$

where T_{GR} indicates the average intensity transmission through the gratings, ψ is the shift of the sinusoidal fringe profile measured with no object in the beam, and $S = p_2/d_{Talbot}$ is the angle corresponding to one grating period; V indicates the fringe visibility, defined as $V \equiv (I_{max} - I_{min})/(I_{max} + I_{min})$, where I_{min} and I_{max} are respectively the minimum and maximum intensities on the fringe profile.

In the case of small refraction angles, such that $\Delta\theta_y \ll S/4$, the function G can be well approximated, in analogy with the ABI case, with a first-order Taylor expansion [24]:

$$I_{GI} \simeq M^{-2} I_0 T_{GR} T \left[G(y_G) + G'(y_G) \Delta \theta_y \right] \tag{6}$$

where $G'(y_G)$ denotes the first derivative of the function G with respect to the refraction angle. The similarity of the signals in the GI and ABI techniques is evident from Eqs. (2-6): both techniques are sensitive to the refraction angle (more precisely to its component along one direction), and in both cases the signal is proportional to the refraction angle if this is sufficiently small. A typical GI signal is plotted in Fig. 1(c), in the case of a simple pure phase object.

Differently from ABI, GI works efficiently even with relatively broad-band radiation [11] but requires a high degree of spatial coherence. It was shown that the technique can also be applied to normal X-ray tubes delivering spatially incoherent radiation if an appropriate third grating is added close to the source [11]. This comes however at the expenses of the available photon flux (and therefore of the time required to acquire an image), since the source grating introduces a considerable filtration of the incoming radiation.

2.1. Spatial resolution

In a real case, the here-considered techniques are characterized by a finite spatial resolution whose value depends on the experimental acquisition parameters. The imaging system point-spread function (PSF) can be approximated as the product of two one-dimensional Gaussian functions:

$$P_{sys} = \left(2\pi \sigma_{sys,x} \sigma_{sys,y} \right)^{-1} \exp \left[-x^2 / 2\sigma_{sys,x}^2 - y^2 / 2\sigma_{sys,y}^2 \right] \tag{7}$$

where $\sigma_{syst,x}^2$ and $\sigma_{syst,y}^2$ represent the PSF variances referred to the object plane, in the x and y directions. Equation (7) takes into account that the spatial resolution can be significantly different in the two image directions. In the case of PBI, the PSF variances can be written as [18]:

$$\sigma_{sys\,PBI,x,y}^2 = \left(M - 1 \right)^2 M^{-2} \sigma_{src,x,y}^2 + M^{-2} \sigma_{det,x,y}^2 \tag{8}$$

where $\sigma_{src,x,y}$ indicates the source size and $\sigma_{det,x,y}$ the width of the detector PSF, respectively in the directions x and y. The first term in Eq. (8) is predominant for large values of the magnification factor ($\sigma_{sys,PBI} \approx \sigma_{src}$ if $M \to \infty$), while the second term is more important when the magnification is small ($\sigma_{PBI,sys} \approx \sigma_{det}$ if $M \to 1$). There is therefore a limit for the spatial resolution in PBI, depending on the particular value of the magnification factor. In the general case, the resolution is also limited by the width of the first Fresnel zone but in the near-field diffraction regime, as shown by Gureyev and associates [18], the latter is much smaller than the width of the system PSF.

Equation (8) is also valid for GI. However, it has to be noted that in this case there is a low limit in the size of the detector pixels: they are required to be at least the size of an entire period of the second grating, at least in the direction y perpendicular to the grating lines.

The PSF variances for ABI in the x and y directions can be written instead as:

$$\sigma_{sys\,ABI,x}^2 = \left(M - 1 \right)^2 M^{-2} \sigma_{src,x}^2 + M^{-2} \sigma_{det,x}^2 \tag{9}$$

$$\sigma_{sys\,ABI,y}^2 = \left(M - 1 \right)^2 M^{-2} \sigma_{src,y}^2 + M^{-2} M_{asym}^{-2} \sigma_{det,y}^2 + M^{-2} M_{asym}^{-2} \sigma_{an,y}^2 \tag{10}$$

where an additional source of spatial resolution degradation, due to the intrinsic PSF of the analyzer crystal, is present in the direction y parallel to the diffraction plane. The blurring

introduced by the analyzer can be essentially attributed to the finite penetration length of X-rays in the crystal, and its width can have values of up to a few micrometers. This blurring can however be reduced (to values in the submicrometre range) with the use of asymmetrically-cut crystals, characterized by a magnification factor $M_{asym} > 1$ [23].

3. Definition of signal-to-noise ratio and figure-of-merit

3.1 Area signal

In the case of an area signal (typical of conventional absorption imaging), the signal-to-noise ratio (SNR) of a detail with respect to the surrounding region (considered as the background) is usually defined as [25]:

$$SNR_{area} \equiv \frac{\sqrt{A}\left(I_{obj} - I_{back}\right)}{\sqrt{std^2\left(I_{obj}\right) + std^2\left(I_{back}\right)}} \simeq \frac{\sqrt{A}\left(I_{obj} - I_{back}\right)}{\sqrt{I_{obj} + I_{back}}} \qquad (11)$$

where $I_{obj} = N_{obj}/A$ and $I_{back} = N_{back}/A$ are the mean intensity values in a given area A respectively in the object/detail and in the background, with N_{obj} and N_{back} being the number of counts on the detector in these two regions; $std(I_{obj})$ and $std(I_{back})$ indicate their standard deviations.

The right-hand side of Eq. (11) can be derived under the conditions of a Poisson noise, for which $std\left(N\right) = \sqrt{N}$; in this latter expression we have implicitly assumed that each detected photon produces one count on the digital detector. We will also consider, for sake of simplicity, a detection efficiency of 100%. These assumptions are however not stringent and the following formulas can be easily extended to more general cases.

The SNR is strongly dependent on the incoming X-ray flux (see Eq. (11)) and, in the presence of pure Poissonian noise, it can be shown to be proportional to the square root of the number of incident photons. Therefore, if images acquired with different photon fluxes need to be compared, the SNR does not represent an appropriate parameter. In order to evaluate the quality of an image independently of the delivered dose used to obtain that image it is convenient to introduce the Figure of Merit (FoM) [26]:

$$FoM \equiv \frac{SNR}{\sqrt{D}} \qquad (12)$$

The FoM is independent of the number of photons because the dose, D, is directly proportional to the X-ray flux for a given sample and energy [27]:

$$D = K_{dose}I_0 \qquad (13)$$

where I_0 indicates the beam intensity before the sample and K_{dose} is a constant that depends in a complicated way on both the imaging system (X-rays energy, irradiation geometry..) and the object (shape, dimensions, composition etc.). Note that in general K_{dose} cannot be calculated analytically but only through Monte Carlo simulations. By combining Eqs. (11-13), the following expression for the area FoM can be obtained:

$$FoM_{area} = \frac{\sqrt{A}\left(I_{obj} - I_{back}\right)}{\sqrt{K_{dose}I_0\left(I_{obj} + I_{back}\right)}} \qquad (14)$$

3.2 Edge signal

In addition to the absorption signal specific of homogeneous regions within the object, phase-contrast images are characterized by a peculiar signal generated at the interfaces (edges) between regions with different refractive indexes (see Fig. 1). Following [16, 19] and in analogy with Eq. (11), it is possible to extend the definition of the SNR to the case of an edge signal as:

$$SNR_{edge\,peak} \equiv \frac{\sqrt{A}\left(I_{\max} - I_{\min}\right)}{\sqrt{2std^2\left(I_{back}\right)}} \simeq \frac{\sqrt{A}\left(I_{\max} - I_{\min}\right)}{\sqrt{2I_{back}}} \qquad (15)$$

where I_{min} and I_{max} are the minimum and maximum intensities of a mean intensity profile across the edge, obtained by averaging the signal over a certain number n of pixel rows in the direction parallel to the edge; A is the area defined as $A = np \cdot p$, where p is the pixel size in each dimension; I_{back} is the average intensity in the background (outside the edge). In Eq. (15) we have again assumed a pure Poissonian noise (like in Eq. (11)).

We will refer to the quantity defined in Eq. (15) as the "*peak edge*" SNR. The corresponding figure of merit can be expressed, by using Eqs. (12-13), as:

$$FoM_{edge\,peak} = \frac{\sqrt{A}\left(I_{\max} - I_{\min}\right)}{\sqrt{2K_{dose}I_0 I_{back}}} \qquad (16)$$

The previous definitions of peak edge SNR and FoM do not actually consider the width of the edge. The latter parameter, however, can be important with respect to the detail visibility. For this reason, an alternative definition for the edge signal has been introduced by Gureyev and associates [18]; it takes into account not only the maximum and minimum intensity values but the integral of all the values across the edge (see Fig. 1).

Supposing an edge extended on the x direction (perpendicular to the sensitivity direction of ABI and GI techniques), the integral edge SNR and FoM for the three here studied phase-contrast methods can be written as:

$$SNR_{\mathrm{int}.edge} \equiv \frac{\int_{-a}^{+a} dy \int_{x_0}^{x_1} dx \left| I\left(x, y\right) - I_{back}\right|}{\sqrt{2\int_{-a}^{+a} dy \int_{x_0}^{x_1} dx I_{back}}} \qquad (17)$$

$$FoM_{\mathrm{int}.edge} = \frac{\int_{-a}^{+a} dy \int_{x_0}^{x_1} dx \left| I\left(x, y\right) - I_{back}\right|}{\sqrt{2K_{dose}I_0 \int_{-a}^{+a} dy \int_{x_0}^{x_1} dx I_{back}}} \qquad (18)$$

where $2a$ represents the edge width (in the y direction) and $L_x = x_1 - x_0$ the width, in the direction parallel to the edge, considered for calculating the average edge profile. We will henceforth refer to the above-defined quantities as the "*integral edge*" SNR and FoM.

4. Calculation of figure of merit

In the following, analytical expressions for the FoM will be derived for the PBI, ABI and GI techniques, respectively. Both area and edge signals will be analyzed. For sake of simplicity, the effect of magnification will be here neglected.

4.1 Calculation of area FoM

In addition to the phase effects at the edges of an object/detail, phase-contrast images also show a signal due to X-ray attenuation, similar to that encountered in conventional X-ray imaging. This signal gives rise to an area contrast, visible in the bulk region of objects, which provides complementary information to the phase signal.

In order to derive the FoM for the area signal in PBI, we consider a region in the object where the phase signal is absent. By inserting Eq. (1) into Eq. (14), the following expression can be obtained:

$$FoM_{PBI,abs} = \frac{\sqrt{A}\left[\exp\left(-\int dz\mu_{obj}\right) - \exp\left(-\int dz\mu_{back}\right)\right]}{\sqrt{K_{dose}\left(\exp\left(-\int dz\mu_{obj}\right) + \exp\left(-\int dz\mu_{back}\right)\right)}} \approx \frac{\sqrt{A}\left(\int dz\mu_{back} - \int dz\mu_{obj}\right)}{\sqrt{K_{dose}\left(2 - \int dz\mu_{back} - \int dz\mu_{obj}\right)}} \quad (19)$$

The approximation on the right side of Eq. (19) is valid only in the case of small absorption, such that $\int dz\mu \ll 1$. It can be noted that Eq. (19) is similar to the FoM that one would obtain in absorption imaging. The important difference is that in the latter case the Compton-scattered X-rays can blur the detected signal and can introduce additional noise in the image (a well-known problem in conventional radiology [28]). In PBI instead, thanks to the propagation distance r between the sample and the detector, the X-rays scattered at a sufficiently large angle will not reach the detector, and the blurring due to Compton scattering can be largely reduced (analogously to the scatter rejection method by air gaps which can used in conventional diagnostic radiology [29]).

From Eq. (19) we can remark that the FoM (in the case of dominant Poissonian noise) is independent of the photon flux I_0 incident on the sample. This confirms that the FoM is an appropriate quantity for comparing the quality of images acquired with different incoming photon fluxes (or, equivalently, at different doses to the sample).

The area FoM in ABI can be calculated from Eqs. (2) and (14), by considering a region where the refraction angle $\Delta\theta_y$ is equal to zero. It can be easily shown that:

$$FoM_{ABI,abs} = \sqrt{R(\theta_{an})}FoM_{PBI,abs} \quad (20)$$

$R(\theta_{an}) < 1$, thus the value of the area FoM for a pure absorbing object is smaller than in the case of PBI. This is a direct result of the filtration introduced by the analyzer crystal, which reduces the number of photons impinging on the detector. This means that, for the same number of photons exiting the sample, in ABI the photon statistics recorded on the detector is reduced and the relative contribution of noise is more important. An advantage of ABI, however, is the total rejection of the Compton-scattered X-rays by the analyzer.

A similar expression for the area FoM can be obtained for the GI technique from Eqs. (6) and (14):

$$FoM_{GI,abs} = \sqrt{T_{GR}G(y_G)}FoM_{PBI,abs} \quad (21)$$

Like in ABI, there exists in GI a considerable photon filtration due to the absorption in the two gratings (particularly in the second one, which is usually made of highly absorbing stripes with duty cycle ~0.5). This fact results in an unavoidable reduction in the FoM values

for the attenuation signal. Furthermore, it can be noted that, in GI, the beam intensity on the detector depends also, through the function $G(y_G)$, on the considered working point y_G.

Compton-scattered photons are mostly rejected in GI because of the non-zero distance between the sample and the detector, and the beam filtration operated by the gratings.

4.2 Calculation of peak edge signal FoM

In PBI the peak edge FoM can be derived by simply combining the general equation for the peak edge FoM (Eq. (16)) with that for the intensity incident onto the detector in the near-field regime (Eq. (1)):

$$FoM_{PBI,peak} \simeq -\frac{\lambda d \sqrt{A}}{2\pi\sqrt{2K_{dose}}}\left(\nabla^2_{max}\phi - \nabla^2_{min}\phi\right) \tag{22}$$

In the near-field regime the FoM is thus proportional to the difference between the values of the phase Laplacian at the two sides of the object/detail edge, and to the defocusing distance (if the validity conditions for TIE are still satisfied).

Another important aspect to be considered is the dependence upon the energy (E). In good approximation, the phase shift can be assumed to be inversely proportional to E [1]. As a consequence, the $SNR_{PBI,peak} = \sqrt{I_0 K_{dose}} FoM_{PBI,peak}$ is proportional to $1/E^2$. For the FoM, the energy dependence is instead more complex and cannot be univocally determined: the coefficient K_{dose} depends on both E and the sample geometry and composition, and the two dependencies are correlated.

Under the assumption of refraction angles small compared to the FWHM of the RC, the peak edge FoM for ABI can be derived by combining Eqs. (4) and 16):

$$FoM_{ABI,peak} \simeq \frac{\sqrt{A}}{\sqrt{2K_{dose}}} \frac{R'(\theta_{an})}{\sqrt{R(\theta_{an})}} \Delta\theta_y \tag{23}$$

The FoM is therefore proportional to the refraction angle. The factor $R'(\theta_{an})/\sqrt{R(\theta_{an})}$ that appears in Eq. (23) strongly depends on the chosen analyzer position. This means that, for a given experimental setup, the sensitivity of the technique (and the values of FoM) can be varied and optimized by selecting specific positions of the analyzer along its RC.

Figures 2(a,b,c) show example profiles of the RC, its derivative and the quantity $R'(\theta_{an})/\sqrt{R(\theta_{an})}$, respectively. They were calculated by considering an X-ray energy of 26 keV and the (111) reflection for both a silicon monochromator and a silicon crystal analyzer [30]. Figure 2(b) shows that the first derivative of the RC varies slowly along the two RC slopes for a relatively large range of angles, and reaches its maximum at around ± 10 μrad (close to the end of the two slopes, where the RC is approximately 10% of its peak value). The $R'(\theta_{an})/\sqrt{R(\theta_{an})}$ function, instead, is not constant at the RC slopes but is strongly peaked around ± 10 μrad (Fig. 2(c)). This implies that, for refraction angles sufficiently small for the linear approximation of the RC to hold, the sensitivity is maximized at these points. Evidently, the crystal material and the used reflection also have a strong influence on the sensitivity: configurations with narrower RC will determine increased SNR and FoM.

The dependence of $SNR_{ABI,peak} = \sqrt{I_0 K_{dose}} FoM_{ABI,peak}$ upon the X-ray energy can be derived from Eq. (23), considering that: i) the Darwin width of the crystal is inversely proportional to E, and thus the RC first derivative is approximately proportional to E [31]; (ii) the refraction angle goes as $1/E^2$. It follows then that the SNR is inversely proportional to E. As pointed out

in the case of PBI, also for ABI the FoM dependence on the energy is non-trivial due to the complicated energy dependence of K_{dose}.
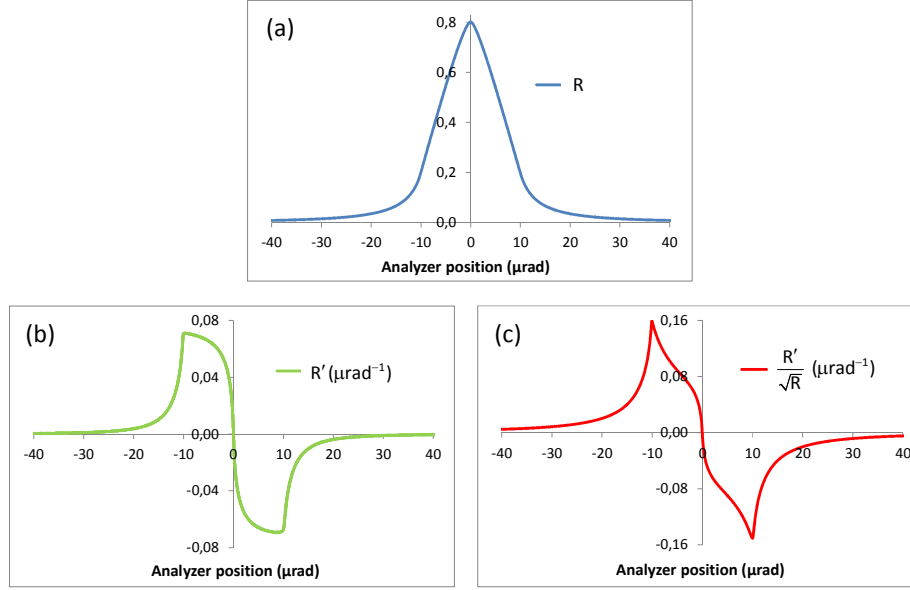

Fig. 2. (a) Profile of the theoretical RC, in the case of monochromator and analyzer in Si(111) Bragg reflection geometry, (b) profile of its first derivative, and (c) ratio between the first derivative and the square root of the RC. All quantities have been calculated with XOP [30] for an X-ray energy of 26 keV.

Finally, an expression that relates the peak edge FoM in GI to the object and setup parameters can be derived by inserting Eq. (6) for the intensity incident on the detector into Eq. (16), which leads to:

$$FoM_{GI,peak} \simeq \frac{\sqrt{AT_{GR}}\,G'\left(y_G;\Delta\theta_y=0\right)}{\sqrt{2K_{dose}G\left(y_G;\Delta\theta_y=0\right)}}\Delta\theta_y = \sqrt{2\pi}\,\frac{\sqrt{AT_{GR}}}{K_{dose}}\frac{Vd_{Talbot}}{p_2}\frac{\cos\left(\psi+\frac{2\pi}{p_2}y_G\right)}{\sqrt{1+\sin\left(\psi+\frac{2\pi}{p_2}y_G\right)}}\Delta\theta_y \quad (24)$$

Similarly to ABI, under the hypothesis of small refraction angles with respect to $S/4$ (with $S = p_2 / d_{Talbot}$ being the angle corresponding to one fringe period), the FoM is proportional to $\Delta\theta_y$. This also implies that, if all the other parameters are unchanged, $SNR_{GI,peak} = \sqrt{I_0 K_{dose}}\,FoM_{GI,peak}$ is inversely proportional to the square of the energy, i.e. $SNR_{GI,peak} \propto 1/E^2$. Furthermore, the SNR and FoM are also inversely proportional to S, thus they are expected to improve with increasing distances d_{Talbot}. However, the visibility V will also decrease with increasing d_{Talbot} because the X-ray beam will never be perfectly coherent. The optimal distance d_{Talbot} corresponding to the maximum value of the FoM is therefore a function of the degree of coherence of the beam.

As in ABI, the value of FoM is strongly dependent on the working point y_G through the function G and its first derivative (see Eq. (24)). The trend of the FoM as a function of the relative gratings position is plotted in Fig. 3(b) over one fringe period. As a reference, the corresponding intensity values along the fringe profile are plotted in Fig. 3(a) and the different positions on the curve are indicated. The points $x = \psi + 2\pi y_G / p_2 = 0$ and $x = \pi$

represent the positions in the middle of the positive and negative slopes, respectively, while the points $x = -\pi/2$ and $x = +\pi/2$ indicate respectively the bottom and the top of the fringe profile. The highest theoretical FoM is achieved at a point that is very close to the half slope where G' is maximized. The choice of the working point is thus very important to optimize the sensitivity in a given setup.
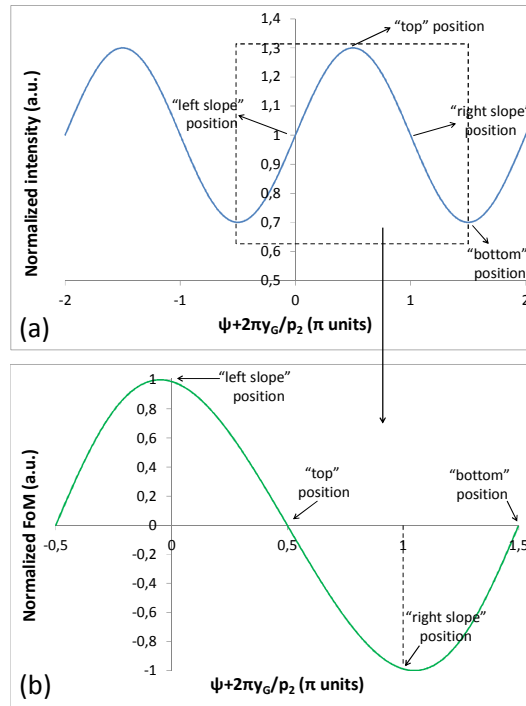

Fig. 3. (a) Intensity profile in GI as a function of the gratings relative displacement, for a visibility of 30%, (b) Normalized FoM values calculated by using Eq. (24) in the range [$-\pi/2$, $3/2\pi$] for the quantity $\psi + 2\pi y_G/p_2$. The different positions on the fringe profile are indicated.

From Eqs. (23-24), we can notice that the ABI and GI techniques are sensitive to a different physical quantity compared to PBI. SNR and FoM in PBI are to first approximation (for small propagation distances and small beam curvature) proportional to the Laplacian of the phase (or, more correctly, to the difference between the values of the phase Laplacian at the two sides of the object/detail edge). In ABI and GI, the SNR and FoM are (for small refraction angles) proportional to the component of the refraction angle on the diffraction plane (ABI) and on the plane perpendicular to the grating lines (GI), respectively.

A direct consequence of the dependence of the PBI signal on the Laplacian of the phase is that this technique is more sensitive to high object frequencies, while ABI and GI are more sensitive to low spatial frequencies, as experimentally shown by Pagot and associates [16].

The comparison of the FoM in ABI and GI is straightforward, because the two techniques are sensitive to the same physical quantity. In the hypothesis that the same object is imaged using the two techniques, from Eqs. (23-24) we can obtain that the ratio of the FoMs is equal to:

$$\frac{FoM_{ABI,peak}}{FoM_{GI,peak}} = \frac{R'(\theta_{an})}{\sqrt{R(\theta_{an})}} \frac{\sqrt{G(y_G; \Delta\theta_y = 0)}}{G'(y_G; \Delta\theta_y = 0)\sqrt{T_{GR}}} \tag{25}$$

Using Eq. (25), for each pair of ABI and GI experimental setups the relative sensitivity of the two methods can be calculated.

Finally, it is noteworthy to remark the different dependence of the three phase-contrast techniques upon the X-ray energy. As we have calculated, $SNR \propto 1/E^2$ in PBI and GI, while $SNR \propto 1/E$ in ABI: this means that ABI is particularly favoured at high energies with respect to the other methods. This different dependence directly follows from the fact that the Darwin width of the crystal is inversely proportional to E, thus the crystal sensitivity is increased at higher energies.

4.3 Calculation of integral edge signal FoM

We will here follow the approach used by Gureyev and associates [18] to calculate the integral edge SNR for PBI, and extend it to the calculation of the FoM in PBI, ABI and GI techniques.

Let us consider the case of an object edge parallel to the x direction, i.e. perpendicular to the direction of sensitivity of ABI and GI techniques. Under the assumption that the recorded intensity is independent of x, Eq. (18) for the FoM can be rewritten as:

$$FoM_{int.edge} = \frac{\sqrt{L_x} \int_{-a}^{+a} dy |I(y) - I_{back}|}{\sqrt{4K_{dose} a I_0 I_{back}}} \tag{26}$$

Let us further assume that the phase profile across the edge can be expressed as:

$$\phi = (H * P_{obj})(y) \phi_{step} \tag{27}$$

where H is the Heavyside step function, ϕ_{step} is the total step of the phase shift across the edge, and $P_{obj} = (2\pi\sigma_{obj,y}^2)^{-1/2} \exp[-y^2/2\sigma_{obj,y}^2]$ is a normalized Gaussian function that expresses the smoothness of the object edge.

If we take into account the effect of the system PSF on the recorded intensity (Eqs. (7-8)), the PBI TIE equation for slowly varying absorption (Eq. (1)) becomes:

$$I(y) - I_{back} \approx -I_0 \frac{\lambda d}{2\pi} \nabla_{\perp}^2 \phi(y) * P_{sys,PBI}(x, y) \tag{28}$$

By using the expression for the phase profile in Eq. (27) and knowing that the derivative of the Heavyside function is the Dirac delta function, the convolution in Eq. (28) can be written as:

$$\nabla_{\perp}^2 \phi * P_{sys,PBI} = \phi_{step} \delta(y) * \partial_y (P_{obj} * P_{sys}) = -\phi_{step} y \exp[-y^2/2\sigma_{PBI}^2] (\sigma_{PBI}^3 \sqrt{2\pi})^{-1} \tag{29}$$

where $\sigma_{PBI}^2 \equiv \sigma_{obj}^2 + \sigma_{sys\,PBI,y}^2$. Finally, by inserting Eqs. (28-29) into Eq. (26), and after tedious calculations, we obtain:

$$FoM_{PBI,int.edge} = \frac{d\lambda\sqrt{L_x}}{2\pi\sigma_{PBI}\sqrt{2\pi K_{dose}}} |\phi_{step}| \frac{1}{\sqrt{a}} \left[1 - \exp\left(-\frac{a^2}{2\sigma_{PBI}^2}\right) \right] \tag{30}$$

It can be shown numerically that the quantity in Eq. (30) is maximized if $a \simeq 2.16\sigma_{PBI}$. A good choice for the value of the integration parameter a in Eq. (26) is $a = 2\sigma_{PBI}$, which is approximately equal to the width of the first Fresnel fringes in the TIE regime. Equation (30) then becomes:

$$FoM_{PBI,\mathrm{int.edge}} \simeq 3.88 \cdot 10^{-2} \frac{d\lambda\sqrt{L_x}}{\sigma_{PBI}\sqrt{\sigma_{PBI}}\sqrt{K_{dose}}}\left|\phi_{step}\right| \tag{31}$$

The corresponding expression for ABI can be similarly obtained. Using a linear approximation for the RC (Eq. (4)), and considering the finite PSF of the imaging system (Eqs. (7, 9 and 10)), we can write:

$$I(x,y) - I_{back} = I_0 R'(\theta_{an})\frac{\lambda}{2\pi}\frac{\partial\phi(y)}{\partial y} * P_{sys,ABI}(x,y) \tag{32}$$

The convolution in Eq. (32) can then be analytically calculated, in a similar way to the case of PBI (with the difference that here the first derivative of the phase needs to be considered):

$$\frac{\partial\phi}{\partial y} * P_{sys,ABI} = \phi_{step}\cdot\delta(y)*\left(P_{obj}*P_{sys}\right) = \phi_{step}\cdot\left(\sqrt{2\pi}\sigma_{ABI}\right)^{-1}\exp\left[-y^2/2\sigma_{ABI}^2\right] \tag{33}$$

where $\sigma_{ABI}^2 \equiv \sigma_{obj}^2 + \sigma_{sys\,ABI,y}^2$. If Eqs. (32-33) are then inserted into Eq. (26), for the integral edge FoM we get:

$$FoM_{ABI,\mathrm{int.edge}} = \frac{\lambda\sqrt{L_x}R'(\theta_{an})\left|\phi_{step}\right|}{4\pi\sqrt{K_{dose}R(\theta_{an})}}\left(\frac{1}{\sqrt{a}}\int_{-a}^{+a}\left(\sqrt{2\pi}\sigma_{ABI}\right)^{-1}\exp\left[-y^2/2\sigma_{ABI}^2\right]\right) \tag{34}$$

In analogy with PBI, we will choose the value $a = 2\sigma_{ABI}$ for the integration parameter a. The Gaussian integral is then equal to about 0.95 and the quantity in the parenthesis is about 0.67. It follows that:

$$FoM_{ABI,\mathrm{int.edge}} \simeq 5.37 \cdot 10^{-2} \frac{\lambda\sqrt{L_x}}{\sqrt{\sigma_{ABI}K_{dose}}}\frac{R'(\theta_{an})}{\sqrt{R(\theta_{an})}}\left|\phi_{step}\right| \tag{35}$$

Since the expression for the intensity in GI has mathematically the same form as the ABI one, the same procedure for the calculation of the integral edge FoM can be applied. We obtain then:

$$FoM_{GI,\mathrm{int.edge}} \simeq 5.37 \cdot 10^{-2} \frac{\lambda\sqrt{L_xT_{GR}}}{\sqrt{\sigma_{GI}K_{dose}}}\frac{G'(y_G)}{\sqrt{G(y_G)}}\left|\phi_{step}\right| \tag{36}$$

with $\sigma_{GI}^2 \equiv \sigma_{obj}^2 + \sigma_{sys\,GI,y}^2$.

We now compare the results for the integral edge FoM obtained for the three techniques, by focusing on the different dependences upon the experimental parameters.

Expressions derived for ABI (Eq. (35)) and GI (Eq. (36)) are very similar. In the hypothesis that the same object is imaged using the two techniques the ratio between the two FoMs is easily found to be:

$$\frac{FoM_{ABI,\mathrm{int.edge}}}{FoM_{GI,\mathrm{int.edge}}} = \sqrt{\frac{\sigma_{GI}}{\sigma_{ABI}}}\frac{R'(\theta_{an})}{\sqrt{R(\theta_{an})}}\frac{\sqrt{G(y_G)}}{\sqrt{T_{GR}}G'(y_G)} \tag{37}$$

From Eq. (37) and Eq. (25), one can infer that the relative sensitivity of the ABI and GI techniques is the same as that calculated by considering the peak edge signal, apart from the

dependence upon the square root of σ_{GI}/σ_{ABI}. The latter, however, does not generally play an important role since the spatial resolutions in the two systems do not differ considerably in typical experimental setups.

As we will see in the following, the formulas derived for the integral edge FoM allow a direct comparison of the ABI and GI signals with the PBI one. To do so, let us consider, for instance, the ratio between the ABI and PBI FoMs:

$$\frac{FoM_{ABI,\text{int}.edge}}{FoM_{PBI,\text{int}.edge}} \simeq 1.38 \frac{R'(\theta_{an})}{\sqrt{R(\theta_{an})}} \frac{1}{d} \frac{\sigma_{PBI}\sqrt{\sigma_{PBI}}}{\sqrt{\sigma_{ABI}}} \tag{38}$$

This ratio increases with the X-ray energy, since $R'(\theta_{an})$ is proportional to E. Furthermore, the explicit dependence upon the spatial resolution allows drawing some important considerations on the relative strength of PBI and ABI (or GI) signals. In particular, it can be seen from Eq. (38) that the ABI technique (as well as GI) provides a better FoM than PBI in the case of large values of the PSF width, while PBI is advantageous for small values of this parameter.

To make this comparison even more explicit, let us assume that the same object edge is imaged in two ABI and PBI setups that use the same detector, and that the spatial resolution is dominated by the detector PSF (σ_{det}). Under these hypotheses, $\sigma_{PBI} = \sigma_{ABI} = \sigma_{\text{det}}$ and therefore the ratio in Eq. (38) is proportional to the detector PSF. This means that the relative strength of PBI and ABI signals can be completely reversed by just changing the pixel size: small pixel sizes will provide better values for PBI, larger ones for ABI. Note that a similar situation arises when the total value of the spatial resolution is dominated by the object smoothness σ_{obj} (i.e. $\sigma_{PBI} = \sigma_{ABI} = \sigma_{obj}$): PBI will provide better sensitivity for very sharp details while ABI for smoother ones.

Intuitively, the fact that the signal in PBI is much more dependent on spatial resolution than in ABI and GI (cf. Equations (31, 35-36)) can be explained as follows. In ABI and GI, an edge between two materials with different refractive indexes is characterized by a signal that is either positive or negative. In other words, only one peak (positive or negative) is present at the edge (Fig. 1(c)). In the case of PBI, instead, a positive as well as a negative peaks are always encountered, if the spatial resolution is sufficiently good to allow distinguishing them (Fig. 1(b)). When the ideal edge profile is convolved by the system PSF, the two peaks may rapidly cancel out each other. On the contrary, in ABI and GI, the convolution with the PSF only results in the signal being spread out, but the total integral value under the peak remains the same.

Even if this property was already experimentally known, this concept had not been yet derived and formalized in the literature.

The expressions for the peak edge FoM and the integral edge FoM that have been obtained for the three considered phase-contrast techniques are summarized in Table 1.

Table 1. Peak edge FoM and integral edge FoM calculated in PBI, ABI and GI techniques.

	FoM$_{peak\ edge}$	FoM$_{int.edge}$
Propagation-based imaging (PBI)	$-\dfrac{\lambda d \sqrt{A}}{2\pi\sqrt{2K_{dose}}}\left(\nabla^2_{max}\phi - \nabla^2_{min}\phi\right)$	$3.88\cdot10^{-2}\dfrac{d\lambda\sqrt{L_x}}{\sigma_{PBI}\sqrt{\sigma_{PBI}K_{dose}}}\left|\phi_{step}\right|$
Analyzer-based imaging (ABI)	$\dfrac{\sqrt{A}}{\sqrt{2K_{dose}}}\dfrac{R'(\theta_{an})}{\sqrt{R(\theta_{an})}}\Delta\theta_y$	$5.37\cdot10^{-2}\dfrac{\lambda\sqrt{L_x}}{\sqrt{\sigma_{ABI}K_{dose}}}\dfrac{R'(\theta_{an})}{\sqrt{R(\theta_{an})}}\left|\phi_{step}\right|$
Grating interferometry (GI)	$\dfrac{\sqrt{AT_{GR}}\,G'(y_G;\Delta\theta_y=0)}{\sqrt{2K_{dose}\,G(y_G;\Delta\theta_y=0)}}\Delta\theta_y$	$5.37\cdot10^{-2}\dfrac{\lambda\sqrt{L_xT_{GR}}}{\sqrt{\sigma_{GI}K_{dose}}}\dfrac{G'(y_G)}{\sqrt{G(y_G)}}\left|\phi_{step}\right|$

5. Conclusions

We have theoretically compared the signals provided by the PBI, ABI and GI phase-contrast techniques. The spatial resolutions obtainable by the three methods have been evaluated and compared, as a function of the setup and acquisition parameters, like the source size, the magnification factor and the detector point-spread function (PSF). Additionally, the spatial resolution was also shown to be affected in ABI by the PSF of the analyzer crystal, while in GI it is limited to at least the size of an entire grating period.

Definitions for the signal-to-noise ratio (SNR) and for the figure of merit (FoM) have been provided in both the cases of area and edge signals. FoM has been shown to be the most appropriate quantity when comparing images obtained with different amounts of radiation dose delivered to the sample, because it is independent of the incoming photon flux.

For each of the here-considered techniques, we have obtained analytical expressions that relate in a simple way the FoM to quantities depending on the object and on the experimental setup and acquisition conditions.

We proved that the FoM values for the absorption signal in phase contrast images are different from those that would be obtained in conventional imaging for the same object. The attenuation of the beam between the sample and the detector introduced by the gratings (in GI) or by the analyzer crystal (in ABI) reduces the number of counts on the detector and accordingly the FoM values. On the other hand, the complete and partial Compton scattering rejection in ABI and in GI and PBI, respectively, eliminates or reduces a source of noise typical of conventional absorption imaging.

Two different definitions for the edge FoM have been introduced: the so-called peak edge FoM takes into account only the maximum and minimum intensity of the signal from an edge, while the integral edge FoM considers the sum of all intensity values across the edge. The two quantities are complementary. The first definition is more suitable when the edge of the detail is large with respect to the imaging system spatial resolution (smooth edge) and when different edges overlap each other. The second definition is more convenient in the cases in which the effect of the finite spatial resolution of the imaging system is important and /or an isolated edge in considered.

The expressions obtained for the peak edge and integral FoMs differ considerably in the PBI technique with respect to ABI and GI. This arises from the different nature of the signals: in PBI the signal is proportional to the phase Laplacian (in the near-field regime approximation), while in ABI and GI it is proportional to the refraction angle (in the approximation of small refraction angles). As a consequence, PBI is expected to have

maximum sensitivity for higher object spatial frequencies than ABI and GI do. We also showed that PBI is more affected by the system finite spatial resolution than the other techniques: it provides higher FoM when the width of the PSF is very small, but when the PSF width is increased the positive and negative peaks across the edge cancel each other and the FoM values rapidly decrease.

Important analogies exist between the signal in the ABI and GI techniques. In both cases the peak edge FoM is to first approximation proportional to the refraction angle. The peak edge and integral FoMs are also proportional to the first derivative of the rocking curve (in ABI) and of the function G (in GI). Therefore, the sensitivity is maximized around the slopes of these functions, where their first derivative is maximum, and reaches the lowest values at the top and bottom positions, where the derivative is equal to zero.

We have demonstrated that the sensitivities of the three here-considered techniques present a different dependence upon the energy. The SNR is inversely proportional to the square of the energy ($SNR \propto 1/E^2$) in PBI and GI, while it is inversely proportional to the energy ($SNR \propto 1/E$) in ABI. This means that ABI is particularly favoured with respect to the other techniques if high energies are used.

In this study, the PBI, ABI and GI methods have been compared for the first time in the literature, and a comprehensive analysis of the different area and edge SNR and FoM has been carried out. We believe that the here presented formalism involving three of the most used phase-contrast imaging techniques may find widespread applications. On the one hand, the different definitions that have been given for the SNR and the FoM can be used to quantitatively compare images obtained with different setups and/or experimental parameters. On the other hand, the theoretical expressions that have been obtained for the SNR and FoM are useful in the setting up of experiments, allowing choosing the best technique and experimental parameters according to the properties of the object to be imaged and the experimental requirements (such as dose constraints, the needed spatial resolution etc.).

Acknowledgments